

Magnetic bound states of iron clusters on a superconductor


Silas Amann^{1,*}, Nóra Kucska^{2,*}, András Lászlóffy², Nicolas Néel¹, Balázs Újfalussy², Levente Rózsa^{2,3},
Krisztián Palotás^{2,3,4} and Jörg Kröger^{1,†}

¹*Institut für Physik, Technische Universität Ilmenau, D-98693 Ilmenau, Germany*

²*Department of Theoretical Solid-State Physics, HUN-REN Wigner Research Centre for Physics, Institute for Solid State Physics and Optics, H-1525 Budapest, Hungary*

³*Department of Theoretical Physics, Institute of Physics, Budapest University of Technology and Economics, H-1111 Budapest, Hungary*

⁴*HUN-REN-SZTE Reaction Kinetics and Surface Chemistry Research Group, University of Szeged, H-6720 Szeged, Hungary*

 (Received 31 July 2023; revised 16 October 2023; accepted 17 October 2023; published 2 November 2023)

The magnetic exchange interaction of Fe_n ($n = 1, 2, 3$) clusters with the quasiparticles of superconducting Pb(111) is probed by scanning tunneling spectroscopy of Yu-Shiba-Rusinov states. The spectral weight of the Yu-Shiba-Rusinov resonances is shifted from the coherence peaks in the Fe monomer spectrum towards the Fermi energy in the Fe dimer spectrum. Unexpectedly, the linear Fe trimer does not follow this trend, as it exhibits an almost identical spectrum to the single Fe atom. Kinked Fe trimers where one of the end atoms deviates from the linear orientation, in contrast, show strong Yu-Shiba-Rusinov resonances well within the Bardeen-Cooper-Schrieffer energy gap of the substrate. First-principles simulations of the Yu-Shiba-Rusinov states reveal which adsorption geometries and magnetic structures of the clusters can reproduce the experimental spectra most accurately.

DOI: [10.1103/PhysRevB.108.195403](https://doi.org/10.1103/PhysRevB.108.195403)

I. INTRODUCTION

Yu-Shiba-Rusinov (YSR) states are induced by magnetic impurities in or on conventional superconductors [1–3]. They appear with binding energies inside the Bardeen-Cooper-Schrieffer (BCS) energy gap [4] and were originally observed from spectroscopy of the differential conductance (dI/dV , I : current, V : voltage) of planar tunneling junctions comprising Mn-implanted Pb [5]. Later, a scanning tunneling microscope (STM) was used to infer YSR levels from dI/dV spectra atop single Gd and Mn atoms on superconducting Nb(110) [6]. Using superconducting tips in STM experiments boosts the energy resolution in spectroscopy beyond the Fermi-Dirac limitation and allows the accurate probing of YSR resonances [7]. Research on YSR states was revived by their competition with the Kondo effect [8]. Theoretical and experimental aspects of YSR bound states have been summarized in excellent review articles [9,10].

The general importance of YSR resonances is best evidenced by their potential role in building blocks for topological superconductivity. In magnetic-atom assemblies the resulting YSR bands may be tailored by the actual arrangement geometry and spin texture. Monomers [6,8,11–15] and dimers [7,16–19] of atoms and molecules were therefore analyzed in detail on superconductor surfaces. In addition, the intragap states were proposed as subtle probes for magnetic properties and interactions [20,21]. For instance, the axial anisotropy of single molecules [22], the dependence of the

exchange interaction on the molecular configuration [23] and the emergence of a spin moment of otherwise diamagnetic molecules in a molecular environment [24,25] were probed along the lines of the theoretical predictions [20,21]. It was moreover shown that the position of YSR resonances inside the BCS energy gap is determined by the exchange coupling of the magnetic moment to the Cooper pair condensate of the substrate [1–3,8], their number is related to spin-polarized orbitals [12,13] and spin multiplets in case of magnetic anisotropy [11], while their splitting and hybridization into bands is governed by the exchange interaction between neighboring magnetic atoms [26]. A recent work has demonstrated the importance of spin-orbit coupling and the breaking of inversion symmetry for understanding the relation between YSR resonances and the actually underlying magnetic order of the atomic-scale clusters [19].

The main motivation for the work here is the use of YSR resonance spectroscopy to unravel the magnetic structure of atomic clusters. Indeed, the intriguing question whether magnetic order of atomic or molecular arrangements can unequivocally be extracted from the spectroscopy of YSR states has scarcely been addressed [17,19]. In addition, Fe atoms in a honeycomb mesh on Pb(111) were previously proposed to induce two-dimensional superconductivity [27], which partly stimulated to explore the actual magnetic texture of the atomic-scale building blocks of this honeycomb assembly. In the present study, the combination of scanning tunneling spectroscopy (STS) experiments with density functional theory (DFT) simulations based on the Korringa-Kohn-Rostoker (KKR) Green's function method provides suggestions for the atomic spin texture of small Fe_n ($n = 1, 2, 3$) clusters on Pb(111). Spectral data of Fe monomers

*These authors contributed equally to this work.

†joerg.kroeger@tu-ilmenau.de

indicate the presence of YSR states by a small asymmetry of the Pb(111) BCS coherence peaks, while for Fe dimers the intragap states are signaled by shoulders to the coherence peaks, i.e., by YSR states with slightly decreased binding energy. Surprisingly, this trend of shifting of the YSR resonances more toward the interior of the BCS energy gap with increasing cluster size is not continued by linear Fe trimers, ℓ -Fe₃. Rather, their spectrum is essentially identical with the monomer data; that is, the presence of YSR levels is indicated by the asymmetry of peak heights at the gap edge. In kinked Fe trimers, k -Fe₃, where one of the end atoms does not follow the residual dimer direction, YSR resonances are clearly visible inside the BCS pairing gap. This apparent intimate relation between the size, shape and adsorption geometry of the cluster on the one hand and its magnetic order on the other is supported by accompanying KKR Green's function calculations. The Fe adsorption sites in the clusters, their atomic magnetic moments as well as the magnetic structure of the different Fe atom assemblies derived from DFT calculations using the Vienna *ab initio* simulation package (VASP) [28,29] serve as input for subsequent KKR Green's function simulations that help interpret the experimental observations of YSR states. The presented studies therefore also contribute to benchmark state-of-the-art first-principles simulations of YSR states against experimental data.

II. EXPERIMENTAL AND THEORETICAL METHODS

The experiments were carried out with a low-temperature (5 K) STM operated in ultrahigh vacuum (10^{-9} Pa). Clean crystalline Pb(111) surfaces were prepared by repeated Ar⁺ bombardment and annealing. Adsorption of individual Fe atoms proceeded via electron-beam evaporation from a Fe rod (purity: 99.99%) and exposing the cold (8 K) sample mounted in the STM to the flux of atoms passing through openings of the radiation shields of the bath cryostat. Tips were fabricated from a Pb wire (purity: 99.99%, diameter: 250 μ m) and further prepared by repeated indentations into the substrate surface and by single-atom transfer [30–35]. Only those tips were used that yielded the BCS energy gap with coherence peaks at bias voltages $\pm(\Delta_t + \Delta_s)/e$ (Δ_t , Δ_s : BCS gap widths of Pb tip and substrate, e : elementary charge) in spectra of dI/dV evidencing the superconducting state of the tip [Fig. 1(a)]. Clusters of Fe were fabricated by thermally activated monomer diffusion and their occasional fusion. Based on the apparent size and shape of the clusters in STM images (insets of Fig. 1), four types of Fe atom assemblies were distinguished, i.e., single atoms (Fe₁), dimers (Fe₂), linear (ℓ -Fe₃), and kinked (k -Fe₃) trimers. Topographic STM data were acquired in the constant-current mode with the bias voltage applied to the sample. For spectroscopy of dI/dV the dc sample voltage was sinusoidally modulated [root-mean-square (rms) amplitude: 50 μ V_{rms}, frequency: 700 Hz]. The first harmonic of the ac current response of the tunneling junction was detected with a lock-in amplifier.

Relaxed adsorption geometries of the Fe atom assemblies on Pb(111) together with their magnetic texture were calculated using the VASP [28,29] code within DFT with the Ceperley-Alder local density approximation [36]. The calculated geometric and magnetic structure of the different Fe

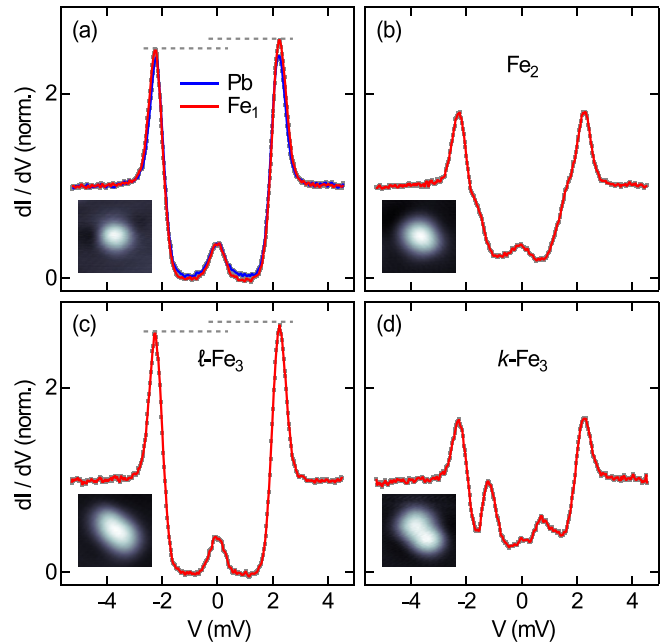


FIG. 1. Spectra of dI/dV acquired atop the center of (a) a single Fe atom (Fe₁), (b) an Fe₂ cluster, (c) a linear and (d) a kinked Fe₃ cluster. Experimental data appear as dots while the solid lines present smoothed data as a guide to the eye. In (a), a spectrum of clean Pb(111) is added. The dashed lines in (a) and (c) indicate the asymmetric height of gap edge peaks in the case of the Fe₁ and ℓ -Fe₃ spectra. For comparison, the spectroscopic data were normalized to unity at ± 5 mV. Feedback loop parameter for all spectra: 5 mV, 100 pA. Insets to (a)–(d): STM images of respective clusters (100 mV, 100 pA, 2.5 nm \times 2.5 nm).

atom clusters then entered into additional calculations to shed light onto the occurrence of YSR states induced by the magnetic exchange interaction of the clusters with the Cooper pair condensate. To this end, the fully relativistic Kohn-Sham-Dirac-Bogoliubov-de Gennes equations were solved in the superconducting state at zero temperature using the KKR Green's function method [37]. Details are summarized in Appendix A.

III. RESULTS AND DISCUSSION

Figure 1 presents the main experimental findings of this work, i.e., the dI/dV spectra of differently sized and shaped Fe clusters. All spectra have in common a zero-bias resonance, which results from thermally induced quasiparticle tunneling between the superconducting Pb tip and the substrate because the width of the Fermi-Dirac function at the experimental sample temperature T_s , $4 k_B T_s \approx 1.72$ meV (k_B : Boltzmann constant) for $T_s = 5$ K, is similar to the BCS energy gap width of Pb [$2\Delta_s(T_s) \approx 2.20$ meV].

The dI/dV spectrum of an Fe monomer [red in Fig. 1(a)] deviates slightly from the spectrum of clean Pb(111) [blue in Fig. 1(a)] in that the peaks at the gap edges at $\pm(\Delta_t + \Delta_s)/e = \pm 2.20$ mV are asymmetric. Defining the asymmetry ratio as $\eta_j = (H_j^+ - H_j^-)/(H_j^+ + H_j^-)$ with H_j^\pm the YSR resonance heights at positive and negative bias voltages observed in the dI/dV data of the clusters ($j = 1, 2, \ell 3, k 3$ for

the monomer, dimer, linear and kinked trimer, respectively), the statistical analysis of 76 Fe monomer spectra results in $\eta_1 = (1.7 \pm 0.9)\%$, i.e., in a positive asymmetry. An asymmetry in the spectra of clean Pb(111) has not been identifiable because a statistical analysis of ten spectroscopic data sets for Pb(111) gave rise to an asymmetry of $(0.3 \pm 0.7)\%$. Therefore the asymmetry visible in the Fe monomer spectra is assigned to a pair of YSR resonances close to the BCS coherence peaks. It was previously demonstrated that the asymmetry in the spectral weight of YSR states reflects the different particle and hole spectral weights caused by the scalar Coulomb potential of the impurity [9]. Asymmetries in the normal-state conductance of the superconductor [38–40] are less important here because the dI/dV spectra are symmetric in the relevant bias voltage range around 0 V. The YSR binding energy ε is determined by the exchange interaction. In a semiclassical description of the single-spin problem, one finds $\varepsilon = \Delta_s(1 - q^2)/(1 + q^2)$ ($q \propto SJ$ with S the single-impurity spin and J the exchange coupling constant) [1–3,41]. Therefore, because the monomer dI/dV spectra suggest $|\varepsilon_1| \approx \Delta_s(T_s) = 1.10$ meV relative to the Fermi energy (E_F), a weak magnetic exchange coupling of the Fe monomer magnetic moment to the Cooper pair condensate may be inferred. From the experimental data alone it is difficult to determine whether the intragap state is unoccupied ($\varepsilon_1 > E_F \equiv 0$) or occupied ($\varepsilon_1 < 0$). Consequently, here and in the following the absolute value of the binding energy is presented.

Before turning to the spectroscopy of the Fe dimer, it is noteworthy that the presence of neighboring Fe atoms did not influence the monomer spectrum for the investigated mutual distances $d \geq 0.46$ nm (Appendix B, Fig. 8). This observation hints at the rather small spatial extension of YSR states induced by the Fe atom because a hybridization of YSR levels of neighboring Fe atoms would expectedly lead to a shift or splitting of the YSR resonances [7,16–20,42–44]. The strong spatial decay will further be discussed below by the analysis of spatially resolved spectra of Fe dimers and trimers. In addition, dI/dV spectra recorded above different sites of the clusters are very similar (Appendix C, Fig. 9). Therefore, the spectral data of Fig. 1 are restricted to the centers of the clusters.

A typical Fe_2 spectrum acquired atop its center is shown in Fig. 1(b). The heights of the peaks defining the gap edges are symmetric and are therefore interpreted as the residuals of the substrate BCS coherence peaks. Shoulders to the coherence peaks toward the inside of the BCS energy gap are visible at $\approx \pm 1.7$ mV.

The spectral data can be fit by convoluting the numerical derivative of the tunneling current [45,46]

$$I(V) \propto \int \varrho_t(E, \Delta_t, \Gamma_t) \varrho_s(E + eV, \Delta_s, \Gamma_s) \cdot [f(E, T_t) - f(E + eV, T_s)] dE \quad (1)$$

(E : energy of the tunneling electron, f : Fermi-Dirac function, $T_{t,s}$: tip and sample temperature) with a normalized Gaussian of full width at half maximum (FWHM) $2\sqrt{2 \ln 2} w_G$ that substitutes the more complicated modulation broadening function. The transmission factor is omitted here because spectral data are evaluated in a small bias voltage range

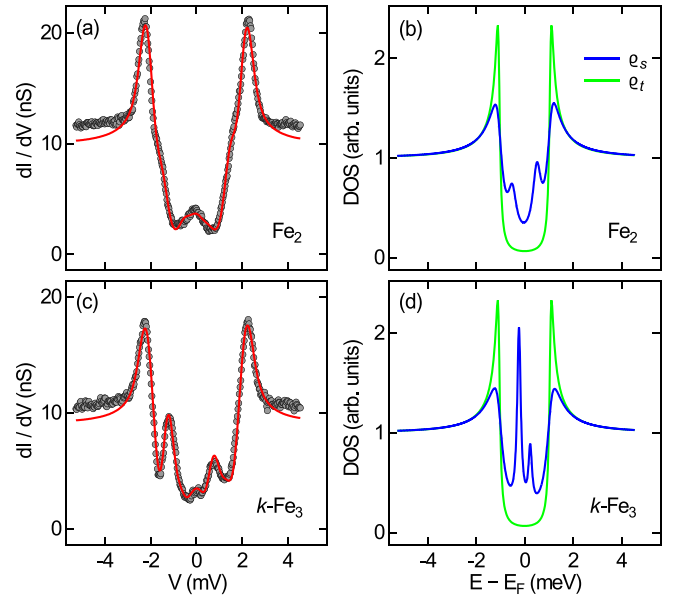


FIG. 2. (a) Spectrum of dI/dV (dots) acquired atop a Fe_2 cluster center together with a fit (solid line). Fit parameters [see text, Eqs. (1)–(3) for explanations]: $\Gamma_t = 71.1 \mu\text{eV}$, $\Gamma_s = 215.7 \mu\text{eV}$, $|\varepsilon_2| = 0.52$ meV, $2w_L = 414.0 \mu\text{eV}$, and $2\sqrt{2 \ln 2} w_G = 422.0 \mu\text{V}$. (b) Sample and tip DOS underlying the fit presented in (a). (c) and (d) as (a) and (b) for the kinked Fe_3 cluster. Fit parameters: $\Gamma_t = 71.1 \mu\text{eV}$, $\Gamma_s = 225.5 \mu\text{eV}$, $|\varepsilon_{k3}| = 0.24$ meV, $2w_L = 153.4 \mu\text{eV}$, and $2\sqrt{2 \ln 2} w_G = 422.0 \mu\text{V}$.

around 0 V, where the variation of the transmission factor is negligible. The tip density of states (DOS) is given by the BCS DOS [4]:

$$\varrho_t(E) = \text{sgn}(E) \cdot \Re \left[\frac{E - i\Gamma_t}{\sqrt{(E - i\Gamma_t)^2 - \Delta_t^2}} \right] \quad (2)$$

(Γ_t : depairing factor that accounts for the broadening of ϱ_t due to the finite quasiparticle lifetime [47], $i^2 = -1$), while the sample DOS is the superposition of the BCS DOS and the YSR resonances modeled as Lorentzians, i.e.,

$$\varrho_s(E) = \text{sgn}(E) \cdot \Re \left[\frac{E - i\Gamma_s}{\sqrt{(E - i\Gamma_s)^2 - \Delta_s^2}} \right] + \sum_{j=1}^n \frac{A_j}{\pi w_L} \cdot \frac{w_L^2}{(E - e_j)^2 + w_L^2} \quad (3)$$

($2w_L$: FWHM of Lorentzian). In view of the available experimental data, only a single pair of YSR resonances is considered, i.e., $n = 2$ and $e_1 = -e_2$ for the resonance energies.

The fit result is depicted in Fig. 2(a) together with the contributing components ϱ_t and ϱ_s in Fig. 2(b). The fits to 13 Fe_2 spectra gave rise to an asymmetry of $\eta_2 = (28.6 \pm 11.5)\%$ and a binding energy of the YSR state of $|\varepsilon_2| = (0.52 \pm 0.03)$ meV. The remaining parameters (T_t , T_s , Δ_t , Δ_s) were obtained from fits to spectroscopic data of the clean Pb(111) surface (Appendix D, Fig. 10) and remained fixed for the evaluation of the cluster spectra. Compared to Fe_1 , the YSR resonance pair extracted from dI/dV data of Fe_2 has departed

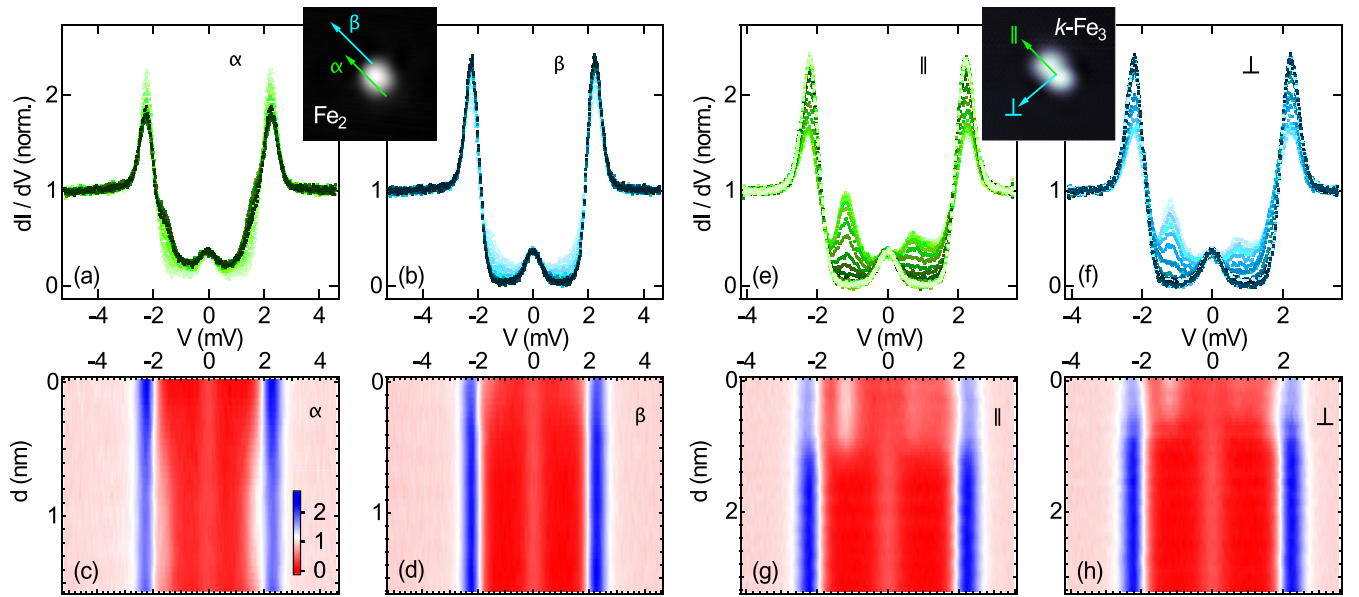


FIG. 3. Spatially resolved dI/dV spectra for a (a)–(d) Fe_2 and a (e)–(h) $k\text{-Fe}_3$ cluster. Inset of (a), (b): STM image of a Fe_2 cluster (10 mV, 50 pA, $4.9 \text{ nm} \times 4.9 \text{ nm}$) with indicated spectroscopy paths α , β oriented parallel to $\langle 1\bar{1}0 \rangle$. The arrows are offset for clarity (the actual α passes across the Fe_2 center and β continues this path from the Fe_2 edge). Inset to (e), (f): STM image of a $k\text{-Fe}_3$ trimer (100 mV, 100 pA, $5.3 \text{ nm} \times 5.3 \text{ nm}$) with spectroscopy paths parallel (\parallel) and perpendicular (\perp) to a $\langle 1\bar{1}0 \rangle$ direction. For the two-dimensional representation of the dI/dV spectra in (c), (d), (g), and (h) the color scale encodes normalized dI/dV values ranging from 0 (red) to 2.5 (blue). Distance $d = 0$ marks the start of the arrows denoted α , β , \parallel and \perp .

from the BCS coherence peaks towards the interior of the energy gap. It is tempting to interpret this observation in terms of an increased magnetic moment of the Fe_2 cluster and its larger magnetic exchange interaction with the Pb Cooper pair condensate. The simulations discussed below lend support to this idea by revealing the ferromagnetic order of the atomic magnetic moments in Fe_2 . Moreover, they reveal that owing to the ferromagnetic interaction in Fe_2 the YSR states of the Fe atom hybridize and shift in energy [20], similar to the experimental observation.

Surprisingly, typical $\ell\text{-Fe}_3$ spectra [Fig. 1(c)] are nearly identical with the Fe_1 spectra; that is, the data indicate the presence of intragap states only by the asymmetry of the coherence peaks. Indeed, for Fe_1 and $\ell\text{-Fe}_3$ convergence of the fits was impeded, presumably due to $|\varepsilon_j| \approx \Delta_s(T_s) = 1.10 \text{ meV}$ ($j = 1, \ell 3$). The extracted asymmetry for the linear trimer is $\eta_{\ell 3} = (1.0 \pm 0.4)\%$, which is based on a statistical analysis of nine spectra. Consequently, the spectroscopic data are indicative of a reduced magnetic moment of the $\ell\text{-Fe}_3$ cluster compared to Fe_2 . A possible explanation of the experimental data is the antiferromagnetic alignment of the atomic magnetic moments in $\ell\text{-Fe}_3$, similar to observations from linear Fe atom chains on Cu_2N surfaces [48]. In addition, YSR states of antiferromagnetically aligned spins exhibit a weaker hybridization than ferromagnetically aligned spins [19,20], which may not lead to a visible change in the measured spectrum compared to the monomer.

Kinked trimers, $k\text{-Fe}_3$, are trimers where one end atom is off the direction defined by the remaining dimer. The dI/dV spectra of $k\text{-Fe}_3$ clusters [Fig. 1(d)] differ strongly from the spectroscopic data of all other clusters. First, the signal strength of the substrate BCS coherence peaks is reduced compared to the Fe_1 and $\ell\text{-Fe}_3$ spectra, even more strongly

than observed for Fe_2 clusters. Second, intragap states are clearly visible and, third, their asymmetry is negative as opposed to the observations of Fe_1 , Fe_2 , and $\ell\text{-Fe}_3$. From fits to the experimental data [Figs. 2(c) and 2(d)] using the same model as for the dimer, an asymmetry of $\eta_{k3} = (-46.2 \pm 3.8)\%$ and a binding energy of the dominant YSR state of $|\varepsilon_{k3}| = (0.24 \pm 0.01) \text{ meV}$ can be inferred. A possible scenario that may be concluded from the experimental data is a ferromagnetic spin texture of $k\text{-Fe}_3$, which leads to a stronger hybridization between the YSR states. The calculations to be discussed below will elucidate the atomic and magnetic structures of the clusters.

The spatial evolution of the spectroscopic signatures related to the YSR states was explored for Fe_2 and $k\text{-Fe}_3$ because these clusters exhibit the clearest signals. For the Fe_2 cluster, spectra were recorded along a path α across the dimer [Fig. 3(a)] as well as along a path β starting from the edge of the cluster and ending on the clean Pb(111) terrace [Fig. 3(b)]. Both paths are oriented parallel to $\langle 1\bar{1}0 \rangle$. To see the changes in the spectra more clearly, the data are represented in two-dimensional plots where the normalized dI/dV signal is converted into a color and plotted as a function of the bias voltage (x axis) and the distance d (y axis) where $d = 0$ is defined by the start of the arrows indicating the paths α , β in the inset of Figs. 3(a) and 3(b). Across the dimer [Fig. 3(c)], the appearance of the intragap states as shoulders to the coherence peaks is visible. Concomitantly with their appearance, the coherence peaks are attenuated. Outside the cluster [Fig. 3(d)], the spectroscopic signature of the YSR state is quickly quenched, within less than 0.5 nm . In particular, an oscillatory decay of the signal strength has not been observed. The kinked $k\text{-Fe}_3$ cluster [Figs. 3(e)–3(h)] exhibits similar spatial characteristics, both parallel [Figs. 3(e) and 3(g)] and

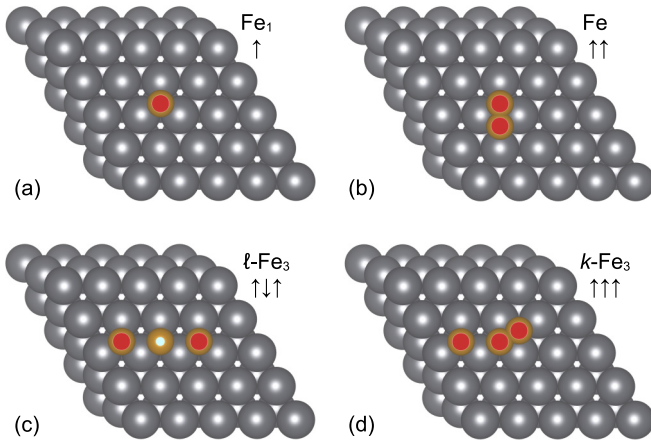


FIG. 4. Relaxed adsorption geometries of Fe clusters on Pb(111) together with their magnetic order. (a) Monomer at hcp lattice site. (b) Dimer occupying hcp and fcc lattice sites. (c) Linear trimer residing at hcp lattice sites. (d) Kinked trimer at two hcp sites and an fcc site.

perpendicular [Figs. 3(f) and 3(h)] to a $\langle 1\bar{1}0 \rangle$ direction. An oscillatory decay of the YSR state signal strength is absent for this cluster species, too. These experimental observations are well supported by the calculations, as discussed below.

Figure 4 shows the DFT-derived configurations of the Fe clusters. For all of these clusters, STM images were calculated in the Tersoff-Hamann approximation [45,46] (Appendix E, Fig. 11). Their agreement with experimental STM topographs supports the applicability of the simulated relaxed adsorption geometries. In the simulations various metastable atomic configurations were found during the relaxation (Appendix A, Table II), which differ in the adsorption sites, the orientation of the clusters, and the distance between the atoms. However, only those calculated structures were considered that gave rise to the best match between experimental and simulated spectra, even in the case where the actual simulated assembly did not represent a minimum-energy configuration.

For the single Fe atom [Fig. 4(a)], the hexagonal close-packed (hcp) Pb(111) adsorption site is favored by 68 meV with respect to the face-centered cubic (fcc) site. The magnetic moment of Fe_1 is $2.57 \mu_B$ and oriented parallel to the surface normal (\uparrow) with an out-of-plane anisotropy energy of 0.38 meV. The Fe atoms of the energetically preferred dimer [Fig. 4(b)] adopt an hcp and the closest fcc site, that is, the Fe dimer is oriented along $\langle 11\bar{2} \rangle$. This result is compatible with the experimental observation where a Fe_2 cluster appears longer along $\langle 11\bar{2} \rangle$ than along $\langle 1\bar{1}0 \rangle$ by a factor of ≈ 1.1 (Appendix E, Fig. 13). The ferromagnetically ($\uparrow\uparrow$) aligned atomic magnetic moments of Fe_2 have a magnitude of $2.45 \mu_B$ (fcc) and $2.50 \mu_B$ (hcp). For the linear $\ell\text{-Fe}_3$ cluster [Fig. 4(c)] the calculations suggest the occupation of adjacent hcp sites as the energetically most favored configuration. The resulting orientation of $\ell\text{-Fe}_3$ clusters along $\langle 1\bar{1}0 \rangle$ directions matches STM data, as shown in Appendix E (Fig. 14). In addition, the atomic magnetic moments of $2.51 \mu_B$, $-2.57 \mu_B$ and $2.51 \mu_B$ are antiferromagnetically ($\uparrow\downarrow\uparrow$) coupled. The kinked $k\text{-Fe}_3$ cluster [Fig. 4(d)] has two Fe atoms residing at adjacent hcp sites while the third atom at one end of the kinked atomic

TABLE I. Summary of DFT-derived properties of the Fe clusters studied in the experiments. The order of the atoms at the adsorption sites, magnetic moments (μ) and texture is the same. The atomic magnetic moments are oriented parallel (\uparrow) or antiparallel (\downarrow) to the Pb(111) surface normal.

Cluster	Adsorption Site	μ (μ_B)	Magnetic Texture
Fe_1	hcp	2.57	\uparrow
Fe_2	hcp; fcc	2.50; 2.45	$\uparrow\uparrow$
$\ell\text{-Fe}_3$	hcp; hcp; hcp	2.51; -2.57 ; 2.51	$\uparrow\downarrow\uparrow$
$k\text{-Fe}_3$	hcp; hcp; fcc	2.45; 2.39; 2.43	$\uparrow\uparrow\uparrow$

chain adopts the closest fcc site. The spin magnetic moments of the Fe atoms align ferromagnetically ($\uparrow\uparrow\uparrow$) with atomic magnetic moments of $2.45 \mu_B$ [hcp, leftmost site in Fig. 4(d)], $2.39 \mu_B$ (adjacent hcp site) and $2.43 \mu_B$ (fcc). This magnetic configuration does not have the lowest energy but it gives rise to the closest match between calculated and experimental STM images as well as calculated LDOS and experimental dI/dV data (see below). Table I summarizes the results for facilitating the comparison.

The key results of the subsequent KKR simulations are displayed in Fig. 5. The calculations of the LDOS were performed at zero temperature with the sample BCS energy gap width set to its maximum value $\Delta_s(0) = 1.36$ meV [49]. To improve the agreement with experimental data, the LDOS at the respective cluster was evaluated in the top vacuum layer where the STM tip probes the electronic structure of the sample [Figs. 5(a)–5(d)]. In addition, the calculated data were convoluted with the BCS DOS of the superconducting tip ($\Delta_t = 1.10$ meV) and further broadened to match the experimental energy resolution [Figs. 5(e)–5(h)]. The calculated LDOS does not exhibit the asymmetry between negative and positive energies observed in the experiments because the electron and the hole components of the LDOS are summed up.

For the Fe monomer, the calculated spectrum exhibits a pair of resonances at ± 1.88 meV [Fig. 5(e)]. These resonances result from the broadening of two individual YSR states with binding energies of $0.56 \Delta_s(0) = 0.76$ meV and $0.69 \Delta_s(0) = 0.94$ meV, which can be seen from the non-broadened LDOS [Fig. 5(a)]. The gap edges in Fig. 5(e) are defined by peaks that are due to the coalescence of the residual BCS coherence peaks and two more YSR states with binding energies of $0.91 \Delta_s(0) = 1.24$ meV and $0.94 \Delta_s(0) = 1.28$ meV [Fig. 5(a)]. The multitude of YSR resonances in the calculations reflects the contribution of several Fe d -orbitals to the bound states. Experimentally, however, the presence of only a single pair of YSR resonances is indicated. In particular, the tunneling process appears to favor those simulated YSR states that are closest to the BCS energy gap edges. A possible rationale is the orbital character of the underlying intragap states. It is reasonable to assume that YSR states resulting from Fe orbitals with orientation along the surface normal (z) overlap particularly well with tip orbitals and lead to a larger dI/dV signal than YSR states that are due to in-plane (x, y) Fe orbitals. The orbital decomposition of YSR

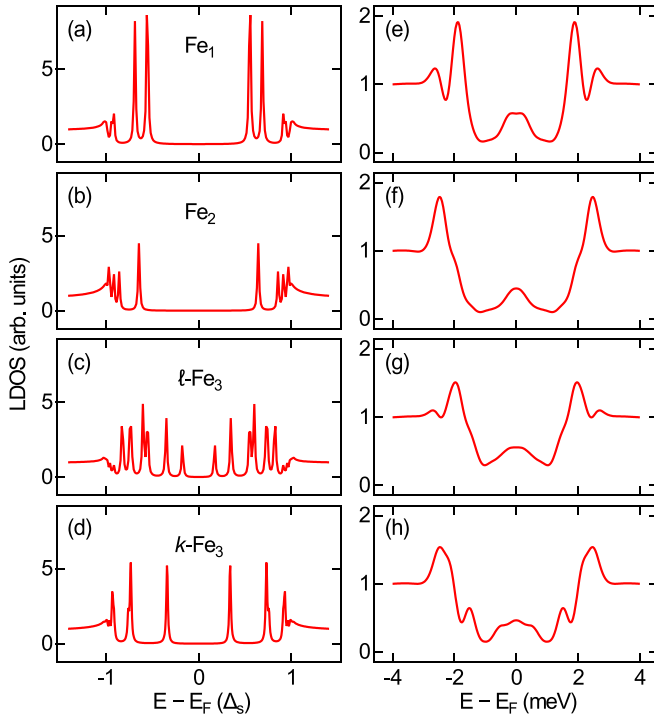


FIG. 5. [(a)–(d)] Calculated LDOS evaluated at $T = 0$ in the vacuum atop the center of the indicated Fe clusters on Pb(111) and (e)–(h) convoluted with the tip BCS DOS using $\Delta_t = 1.10$ meV. The LDOS is normalized to its value at [(a)–(d)] $E - E_F = \pm 1.5 \Delta_s$ and at [(e)–(h)] $E - E_F = \pm 4$ meV. The simulations were performed for (a) and (e) a monomer residing at an hcp site of Pb(111) with 47% inward vertical relaxation, for (b) and (f) a dimer with Fe atoms at adjacent hcp and fcc sites in ferromagnetic alignment, for (c) and (g) a linear trimer occupying adjacent hcp sites and exhibiting antiferromagnetic order, and for (d) and (h) a kinked trimer occupying two hcp sites and the closest fcc site with ferromagnetic alignment. For dimers and trimers the inward vertical relaxation of the individual atoms was chosen to be 40%.

states indeed shows that d_{xz} , d_{yz} and d_{z^2} orbitals contribute strongly to the intragap states with binding energies close to the BCS energy gap edge.

The simulations for the Fe_2 cluster match very well the experimental data. The calculated [Fig. 5(b)] and convoluted [Fig. 5(f)] LDOS gives rise to a spectroscopic shoulder at $\approx \pm 2.0$ meV resulting from a YSR state with binding energy $0.64 \Delta_s(0) = 0.87$ meV, which is compatible with the experimental value. This YSR state has strong contributions from d_{xz} , d_{yz} and d_{z^2} orbitals of the Fe_2 cluster. There are three more YSR states that are grouped close to the BCS gap edges with binding energies of $0.86 \Delta_s(0) = 1.17$ meV, $0.91 \Delta_s(0) = 1.24$ meV and $0.97 \Delta_s(0) = 1.32$ meV. These YSR states do not exhibit similarly pronounced contributions of z -oriented orbitals.

The convoluted and broadened spectrum of the linear $\ell\text{-Fe}_3$ cluster [Fig. 5(g)] is similar to the simulated spectrum of the Fe atom [Fig. 5(e)], which matches the observation of similar dI/dV spectra for $\ell\text{-Fe}_3$ and Fe_1 spectra in the experiments. Dominant peaks occur in the LDOS at ± 1.96 meV, which is slightly closer to the energy gap edges than observed

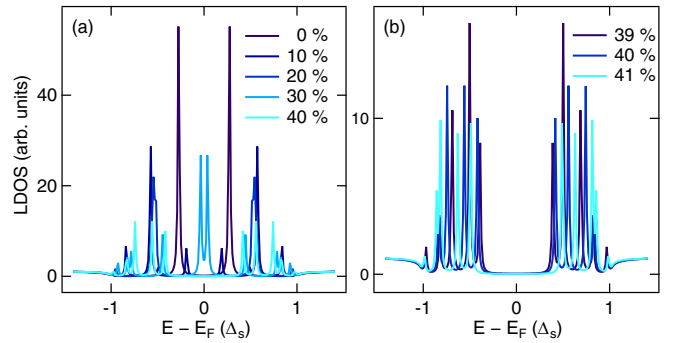


FIG. 6. Adsorption-height dependence of YSR resonances for Fe_1 adsorbed at an hcp Pb(111) site. (a) Calculated LDOS for Fe_1 with inward vertical relaxations ranging between 0% and 40% of the Pb(111) interlayer spacing. (b) As (a), for inward vertical relaxations ranging between 39% and 41%.

for the monomer. These peaks exhibit shoulders that reflect additional YSR resonances. Indeed, a multitude of YSR resonances is present in the nonbroadened LDOS [Fig. 5(c)] at binding energies between $0.18 \Delta_s(0) = 0.24$ meV and $0.95 \Delta_s(0) = 1.29$ meV. The suppression of some of these various states in dI/dV spectra due to their orbital character may explain the deviations from the experimental data.

As observed in the experiments, the broadened LDOS spectrum of the kinked $k\text{-Fe}_3$ cluster [Fig. 5(h)] looks different from the LDOS evolution of the $\ell\text{-Fe}_3$ cluster. A pair of YSR states is positioned clearly inside the energy gap at ± 1.52 meV, which corresponds to a binding energy of $0.34 \Delta_s(0) = 0.45$ meV [Fig. 5(d)], an energy larger than but still comparable with the experimental value. Additional YSR resonances occur in the vicinity of the gap edges with binding energies between $0.73 \Delta_s(0) = 0.99$ meV and $0.93 \Delta_s(0) = 1.26$ meV. These calculated resonance pairs appear to be suppressed in the experiments, which may be assigned to their orbital character. Their close proximity to the energy gap edges may likewise cause their apparent absence because they are no longer resolved in the spectra.

The deviations between simulated and experimental data are most likely due to the atomic adsorption heights in the clusters. The VASP calculations suggest a small nonuniformity of the adsorption heights in the clusters, while in the KKR simulations the same adsorption heights for the individual Fe atoms in a given cluster were assumed due to technical limitations. The strong sensitivity of the LDOS on the adsorption height can be seen for, e.g., Fe_1 in Fig. 6. Changing the inward vertical relaxation in steps of 10% [Fig. 6(a)] or 1% [Fig. 6(b)] of the ideal Pb(111) interlayer distance, the number, energies and LDOS magnitudes of YSR states vary appreciably. Possibly, these changes are due to the fast variations of the normal-state LDOS around E_F . Similarly sensitive YSR resonances were observed for the other Fe clusters, too.

The spatial extent of YSR resonances (Fig. 3) is another relevant information. To see the spatial evolution of the YSR states in the simulations, the LDOS was evaluated in the vicinity of an Fe atom adsorbed on an hcp Pb(111) site with 47% inward relaxation. Figure 7(a) shows the calculated LDOS variation in the Pb(111) surface atomic layer at the nearest Pb

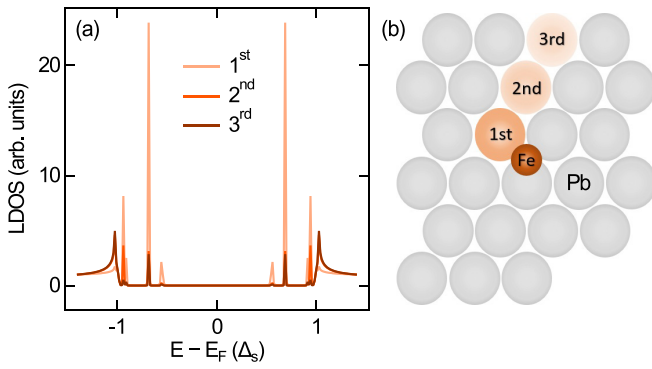


FIG. 7. (a) Calculated LDOS variation in the Pb(111) surface atomic layer at the nearest Pb atom site (first) to the Fe_1 hcp adsorption site as well as neighboring sites (second and third). The Fe_1 inward vertical relaxation is 47% as in Fig. 5(a). (b) Illustration of the Pb(111) lattice sites at which the LDOS in (a) is evaluated.

neighbor (first) to the Fe monomer as well as at neighboring sites (second and third), see Fig. 7(b) for an illustration of the geometry. At the third neighbor, the YSR LDOS is reduced by an order of magnitude. This strong decrease of the LDOS is due to the three-dimensional scattering characteristics underlying the YSR states of Fe clusters on Pb(111). In contrast, for Mn atoms on the same surface, YSR states were shown to spatially extend up to a few nm away from the magnetic atom [12]. This discrepancy possibly hints at the importance of the complex Fermi surface of the superconductor and the spatial profile of the scattering potential for the observation of YSR scattering patterns in STM [50].

Before concluding, a general remark on the comparison between experimental and theoretical data appears to be appropriate. The first-principles calculations are accurate to an extent that reproduces YSR binding energies within fractions of the small Pb superconducting energy gap without any adjustable parameters. The electron-hole asymmetry of YSR resonances observed in the experiments are not reproduced by the calculations because the Bogoliubov-de Gennes equations inherently give rise to symmetric results. Any asymmetry has to result from an additional tunneling theory [17]. With this information in mind, experimental and theoretical results agree satisfactorily well and the main features of the experiment are correctly captured by the calculations. Both experimental and theoretical findings indicate that YSR states appear near the edges of the superconducting energy gap, with the best agreement for the Fe_2 cluster.

IV. CONCLUSION

Spectroscopy of YSR bound states in magnetic nanostructures at superconductor surfaces combined with density functional theory serve as a sensitive tool to probe magnetic order at the atomic scale. For small Fe atom assemblies on Pb(111), the magnetic order depends on size and shape of the cluster and leaves its clear footprint in spectra of dI/dV and of the calculated LDOS. Moreover, adsorption sites and heights of the individual Fe atoms have a profound impact on the spectral data. It will be interesting to explore the spectroscopic

response of YSR states in artificially fabricated heterogeneous structures.

ACKNOWLEDGMENTS

Funding by the Deutsche Forschungsgemeinschaft (Grant No. KR 2912/18-1), the German Federal Ministry of Education and Research within the ‘‘Forschungslabore Mikroelektronik Deutschland (ForLab)’’ initiative, the János Bolyai Research Grant of the Hungarian Academy of Sciences (Grants No. BO/292/21/11 and No. BO/00178/23/11), the National Research Development and Innovation (NRDI) Office of Hungary under Projects No. FK124100, No. K131938, No. FK142601, and No. K142652, the New National Excellence Program of the Ministry for Culture and Innovation from NRDI Fund (Grant No. ÚNKP-23-5-BME-12) is gratefully acknowledged.

APPENDIX A: COMPUTATIONAL DETAILS

1. Density functional theory

Various atomic arrangements and collinear spin configurations of Fe_1 , Fe_2 , and Fe_3 atomic clusters on the Pb(111) substrate were calculated employing the Vienna *ab initio* simulation package (VASP) [28,29]. The local density approximation in the Ceperley-Alder parametrization [36] was used. The face-centered cubic (fcc) Pb(111) surface was modeled as a slab consisting of three atomic layers with a 5×5 surface cell and a surface lattice constant of 0.35 nm. With the exception of the bottom Pb atomic layer, all atomic positions were relaxed during the geometry optimizations until convergence was reached with an atomic force convergence criterion of 0.2 eV/nm. An energy cutoff of 300 eV was used for the plane-wave expansion. A separating vacuum region of at least 2.4 nm thickness avoided unphysical interactions between the repeated image slabs in the perpendicular Pb(111) direction. The Brillouin zone was sampled by the Γ point only.

For Fe_1 , fcc and hcp adsorption sites on the Pb(111) surface were considered. Allowing free relaxation of the Fe atoms in all directions resulted in energetically preferred subsurface Fe_1 positions, which we excluded from further analysis. Instead, the optimization of Fe atoms was further restricted to keep their initial fcc or hcp lateral positions, and out-of-plane movement of the Fe atoms was allowed. This procedure ensured that the Fe atoms stayed on the Pb(111) surface. The same geometry optimization was used for Fe_2 and Fe_3 atomic clusters as well. The resulting total energies and Fe spin moments for selected clusters are summarized in Table II.

For Fe_1 the hcp (h) adsorption site was found to be energetically preferred compared to fcc (f). A mixed fcc-hcp (fh) atomic arrangement with ferromagnetic ($\uparrow\uparrow$) spins gave rise to the lowest total energy for Fe_2 . In the case of the Fe_3 cluster, four types of linear (ℓ) and eight types of kinked (k) atomic arrangements were considered, each in four collinear spin configurations. Among them, many were excluded from further analysis due to comparison with the experiments. Table II reports the total energies and Fe spin moments of selected Fe trimers, which correspond to the experimental findings. Yu-Shiba-Rusinov states of all configurations listed in Table II were calculated. The underlined clusters are included in the

TABLE II. Total energies (E_{tot}) and spin magnetic moments (μ) of Fe_n ($n = 1, 2, 3$) atomic clusters on $\text{Pb}(111)$. The underlined clusters are used in KKR Green's function simulations. Adsorption sites fcc and hcp are abbreviated by f and h, respectively. Spin magnetic moments oriented parallel (antiparallel) to the surface normal are marked as \uparrow (\downarrow). The linear (kinked) Fe_3 cluster is abbreviated as ℓ (k). Lateral Fe–Fe distances are 0.350 nm (h–h) and 0.202 nm (f–h, h–f).

Fe ₁			Fe ₂			Fe ₃		
Site	E_{tot} (eV)	μ (μ_B)	Site	E_{tot} (eV)	μ (μ_B)	Site	E_{tot} (eV)	μ (μ_B)
f(\uparrow)	−309.452	2.59	hh($\uparrow\uparrow$)	−315.877	2.50; 2.50	ℓ -hhh($\uparrow\uparrow\uparrow$)	−322.280	2.40; 2.48; 2.40
<u>h(\uparrow)</u>	−309.520	2.57	hh($\uparrow\downarrow$)	−316.018	2.54; −2.54	ℓ -hhh($\uparrow\uparrow\downarrow$)	−322.402	2.45; 2.56; −2.46
			<u>fh($\uparrow\uparrow$)</u>	−316.837	2.45; 2.50	<u>ℓ-hhh($\uparrow\downarrow\uparrow$)</u>	−322.513	2.51; −2.57; 2.51
			fh($\uparrow\downarrow$) ^a	/	/	ℓ -hhh($\uparrow\downarrow\downarrow$)	−322.402	2.45; −2.52; −2.43
						<u>k-hhf($\uparrow\uparrow\uparrow$)</u>	−323.318	2.45; 2.39; 2.43
						<u>k-hhf($\uparrow\uparrow\downarrow$)</u> ^b	/	/
						<u>k-hhf($\uparrow\downarrow\uparrow$)</u> ^a	/	/
						<u>k-hhf($\uparrow\downarrow\downarrow$)</u>	−323.419	2.50; −2.54; −2.40

^aNo convergence, frustrated state.

^bConvergence to k -hhf($\uparrow\downarrow\downarrow$).

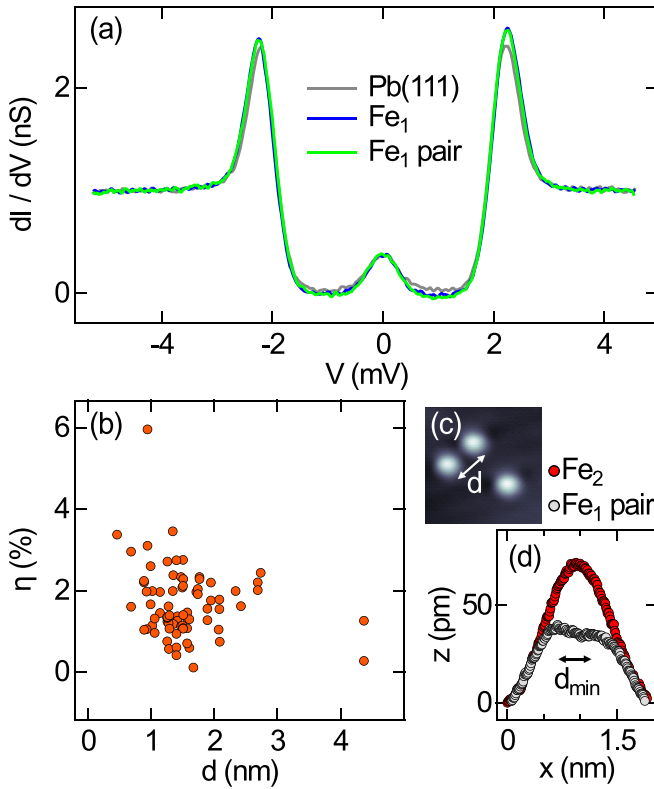


FIG. 8. (a) Spectra of dI/dV acquired atop clean $\text{Pb}(111)$, a single and well separated Fe atom (Fe_1) and a Fe atom with an adjacent Fe atom at 1.75 nm distance (Fe_1 pair). Feedback loop parameters for all spectra: 5 mV, 100 pA. (b) Asymmetries η (dots) extracted from energy gap edge peak heights of Fe monomer dI/dV spectra as a function of distance d between the monomer and a neighboring Fe atom. (c) STM image of three Fe atoms (100 mV, 100 pA, 5.2 nm \times 5.2 nm). Distance d is defined as the separation between the protrusion centers. (d) Cross-sectional profiles of a Fe_2 cluster and an Fe_1 pair with smallest mutual distance d_{min} observed in the experiments. The apparent height z was acquired at tunneling parameters 100 mV and 100 pA.

main manuscript as they provided the best match with the experimental dI/dV results. For the k -hhf Fe_3 cluster the ferromagnetic spin configuration ($\uparrow\uparrow\uparrow$) provided the best match to experimental dI/dV , unlike the energetically favorable $\uparrow\downarrow\downarrow$ spin configuration.

2. Screened Korrington-Kohn-Rostoker Green's function method

The concept of superconductivity can be introduced into DFT by treating the superconducting order param-

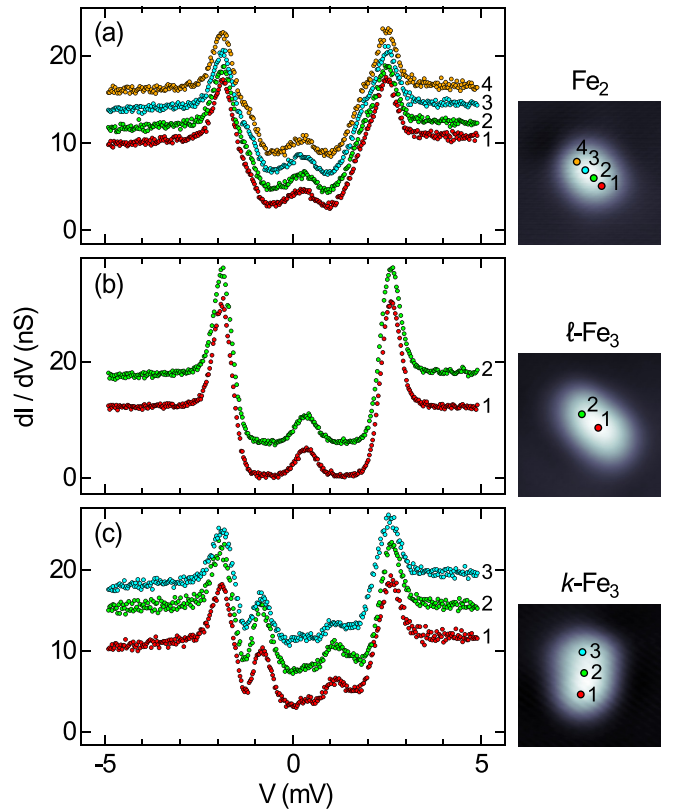


FIG. 9. Spatially resolved dI/dV spectra acquired atop (a) Fe_2 , (b) ℓ - Fe_3 , and (c) k - Fe_3 clusters. The STM images (100 mV, 100 pA, 3 nm \times 3 nm) show the clusters with marked spectroscopy positions. Feedback loop parameters for all spectra: 10 mV, 50 pA.

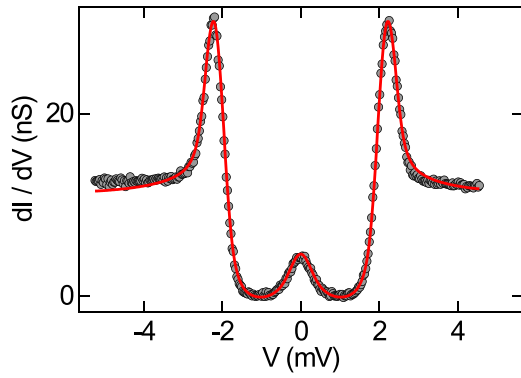


FIG. 10. Fit (solid line) to experimental data (dots) obtained from a clean Pb(111) surface with a Pb tip. Fit parameters [see Eqs. (1)–(3) and explanation in the main article]: $\Delta_s = 1.10$ meV, $\Gamma_s = 71.1$ μ eV, and $2\sqrt{2} \ln 2 w_G = 422.0$ μ V. The resulting sample and tip temperatures are 5 K.

ter as an additional anomalous density [51]. The resulting generalization of Kohn-Sham equations leads to the following Kohn-Sham-Dirac-Bogoliubov-de Gennes (KS-DBdG) Hamiltonian written in Rydberg units:

$$H_{\text{DBdG}} = \begin{pmatrix} H_d & \Delta_{\text{eff}} \\ \Delta_{\text{eff}}^\dagger & -H_d^* \end{pmatrix}, \quad (\text{A1})$$

where the Dirac Hamiltonian reads

$$H_d(\vec{r}) = c\vec{\alpha}\vec{p} + (\beta - \mathbb{I}_4) \frac{c^2}{2} + [V_{\text{eff}}(\vec{r}) - E_F]\mathbb{I}_4 + \vec{\Sigma}\vec{B}_{\text{eff}}(\vec{r}) \quad (\text{A2})$$

with c the velocity of light and

$$\vec{\alpha} = \sigma_x \otimes \vec{\sigma}, \quad (\text{A3})$$

$$\beta = \sigma_z \otimes \mathbb{I}_2, \quad (\text{A4})$$

$$\vec{\Sigma} = \mathbb{I}_2 \otimes \vec{\sigma}, \quad (\text{A5})$$

and $\vec{\sigma}$ the Pauli matrices, \mathbb{I}_j the identity matrix of dimension j , $V_{\text{eff}}(\vec{r})$ and $\vec{B}_{\text{eff}}(\vec{r})$ the effective potential and the exchange field, respectively. The effective 4×4 pairing potential matrix $\Delta_{\text{eff}}(\vec{r})$ is due to the four-component Dirac spinors. The KS-DBdG equations are solved self-consistently by assuming that the superconducting host has isotropic s -wave spin-singlet pairing as described by BCS theory [4].

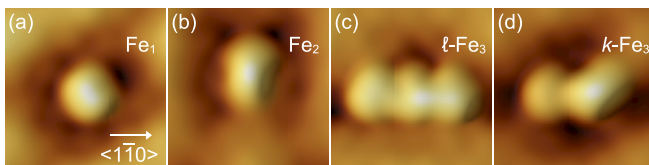


FIG. 11. Calculated STM images ($1.5 \text{ nm} \times 1.5 \text{ nm}$) based on the relaxed adsorption geometries of (a) Fe_1 , (b) Fe_2 , (c) $l\text{-Fe}_3$, and (d) $k\text{-Fe}_3$ (Fig. 4 of the main article). The tip-surface distances range from (a) 0.43, (b) 0.44, (c) 0.46, and (d) 0.47 nm. A $\langle 1\bar{1}0 \rangle$ direction is marked in (a) and applies to (b)–(d), too.

The central quantity of this approach is the Green's function, which is obtained from the generalized multiple scattering theory in a self-consistent way [37]. The advantage of this technique [52] is the exact treatment of semi-infinite geometries (hence the superconducting host) together with the embedding of magnetic atomic clusters without applying a supercell, while naturally providing an accurate treatment of spin-orbit coupling.

For each site of the impurity cluster, the method yields the local Green's function matrix $\{G_{\text{loc}}(z; n, L, L'; s, s'; a, b)\}$ where n denotes the sites of the atomic cluster; $L = (l, m)$ and $L' = (l', m')$ are composed angular momentum indices; s, s' are the spin indices; a, b correspond to either the electronlike or the holelike part of the Green's function. This quantity contains all information about the superconducting ground state involving the description of all the pairing states present in the system. Hence, it allows the calculation of the LDOS, the energy-resolved order parameter, and other related quantities.

The general algorithm for a complete calculation of an impurity cluster is performed according to the following scheme. First, a series of normal-state, conventional DFT calculations are performed within the same Green's function formalism. A bulk calculation provides self-consistent potentials and the Fermi energy for the host (Pb). Then, a normal-state surface calculation is performed to obtain potentials and the vacuum-potential level for the semi-infinite host, Pb(111). Still in the normal state, these computations are followed by an embedded-cluster calculation that gives rise to the self-consistent potentials for the entire impurity cluster, Fe_n ($n = 1, 2, 3$). Second, the same steps are then repeated in the superconducting state, however, without self-consistency. As a result, the superconducting gap of the bulk, of the Pb surface layers as well as the LDOS at the impurity cluster sites is obtained. The superconducting pairing potential is not solved self-consistently; rather, the effective pairing interaction Δ in the KSDBdG equations is set to a value that gives the energy gap for Pb at zero temperature in the bulk DOS calculation, while $\Delta = 0$ is used for the Fe and vacuum sites of the final system. The atomic-sphere approximation is used in the calculations, and induced magnetic moments are neglected that appear on nonmagnetic sites due to their interaction with magnetic sites. These induced moments have been demonstrated to have a minimal influence on the calculated LDOS [37].

APPENDIX B: MONOMER SPECTRUM AND NEIGHBORING FE ATOMS

Spectra of dI/dV of individual Fe atoms in the main article were acquired with a minimum distance to neighboring Fe atoms of 2.5 nm. However, the impact of Fe atoms in the neighborhood of the studied monomer is very weak. Figure 8(a) compares spectra of a well separated monomer (Fe_1) and a monomer with a Fe_1 neighbor at 1.75 nm (Fe_1 pair). Differences are hardly identifiable. Different $\text{Fe}_1\text{-Fe}_1$ distances d were explored and only a small increase of the asymmetry η of the peaks defining the gap edges was observed with decreasing d [Fig. 8(b)]. Figure 8(c) illustrates the definition of the distance d between two Fe atoms. At the minimum distance $d_{\text{min}} = 0.46$ nm observed in the experiments, the individual Fe

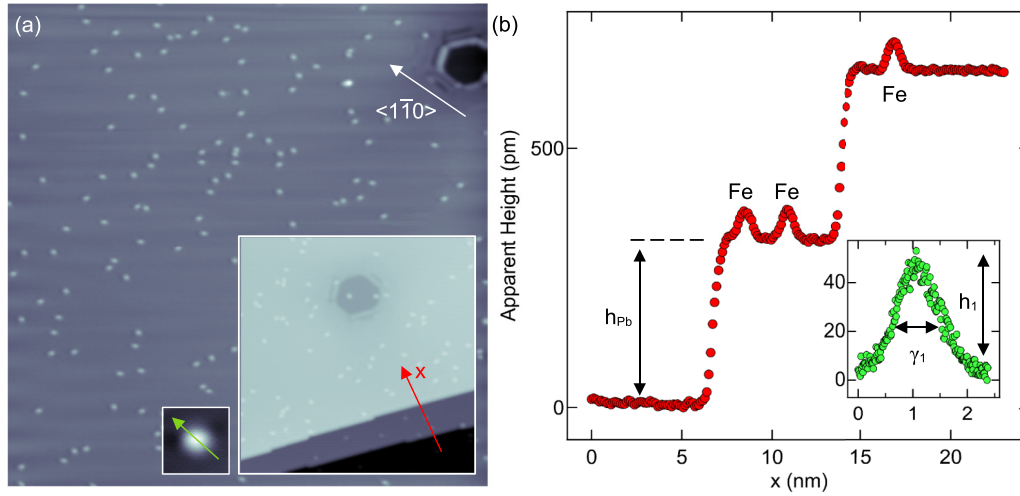


FIG. 12. (a) STM image of Fe-covered Pb(111) (100 mV, 100 pA, 100 nm \times 100 nm). The indicated $\langle 1\bar{1}0 \rangle$ direction coincides with the edge orientation of the interference pattern of a buried cavity (top right). Left inset: STM image (2.5 nm \times 2.5 nm) of a single Fe atom. Right inset: STM image (50 nm \times 50 nm) of three adjacent Pb(111) terraces. (b) Cross-sectional profile acquired atop three adjacent Pb(111) terraces as marked in the right inset to (a). Inset: Cross-section profile recorded above a single Fe atom on Pb(111) as marked in the left inset to (a). The apparent step height was set to $h_{pb} = 284$ pm giving rise to an atom height of $h_1 \approx 45$ pm and to the full width at half maximum $\gamma_1 \approx 0.95$ nm.

atoms still appear as separated protrusions in cross-sectional profiles [Fig. 8(d), lower data set]. A pair of separated Fe_1 with mutual distance d_{min} could be converted into a dimer with increased apparent height and no substructure [Fig. 8(d), upper data set].

APPENDIX C: SPATIALLY RESOLVED SPECTROSCOPY

The main article shows dI/dV spectra that were recorded atop the centers of the Fe clusters. Figure 9 reveals by spatially resolved spectra that differences above the individual Fe atoms of a given cluster are small. Therefore, restriction of spectroscopy above the cluster centers is justified.

APPENDIX D: EXTRACTION OF TIP AND SAMPLE PARAMETERS FROM EXPERIMENTAL SPECTRA

In order to extract binding energies of the intragap states, superconducting parameters of the clean sample and tip must

be available. To this end, the convolution of the numerical derivative of the tunneling current with a normalized Gaussian was fit to experimental data as explained in the main text [Eqs. (1)–(3)]. For the fits of clean Pb(111) spectra, the depairing factor was assumed to be the same for tip and sample, $\Gamma_t = \Gamma_s$. Figure 10 shows an example of such a fit to experimental dI/dV data of clean Pb(111). As expected, the fit resulted in $\Delta_t \approx \Delta_s$ and, thus, $T_t \approx T_s$. For subsequent fits to Fe cluster spectra, these values were kept invariant.

APPENDIX E: ANALYSIS OF FE CLUSTER TOPOGRAPHIES

Constant-current STM images of all Fe clusters were simulated in the Tersoff-Hamann approximation [46] on the basis of relaxed adsorption geometries obtained by density functional calculations (VASP). Figure 11 presents the results for Fe_1 [Fig. 11(a)], Fe_2 [Fig. 11(b)], l - Fe_3 [Fig. 11(c)] and k - Fe_3 [Fig. 11(d)]. The reasonable agreement of the calculated data

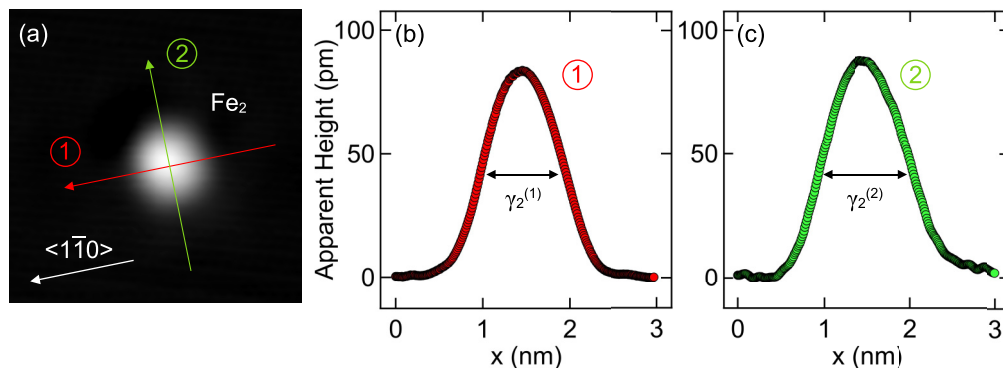


FIG. 13. (a) STM image of a Fe_2 cluster on Pb(111) (10 mV, 50 pA, 4.9 nm \times 4.9 nm). Direction 1 is oriented along $\langle 1\bar{1}0 \rangle$, while 2 is perpendicular to it, i.e., parallel to $\langle 11\bar{2} \rangle$. (b),(c) Cross-sectional profiles acquired along directions 1 and 2 marked in (a) with $\gamma_2^{(1)} \approx 0.99$ nm, $\gamma_2^{(2)} \approx 1.08$ nm, and $h_2 \approx 85$ pm.

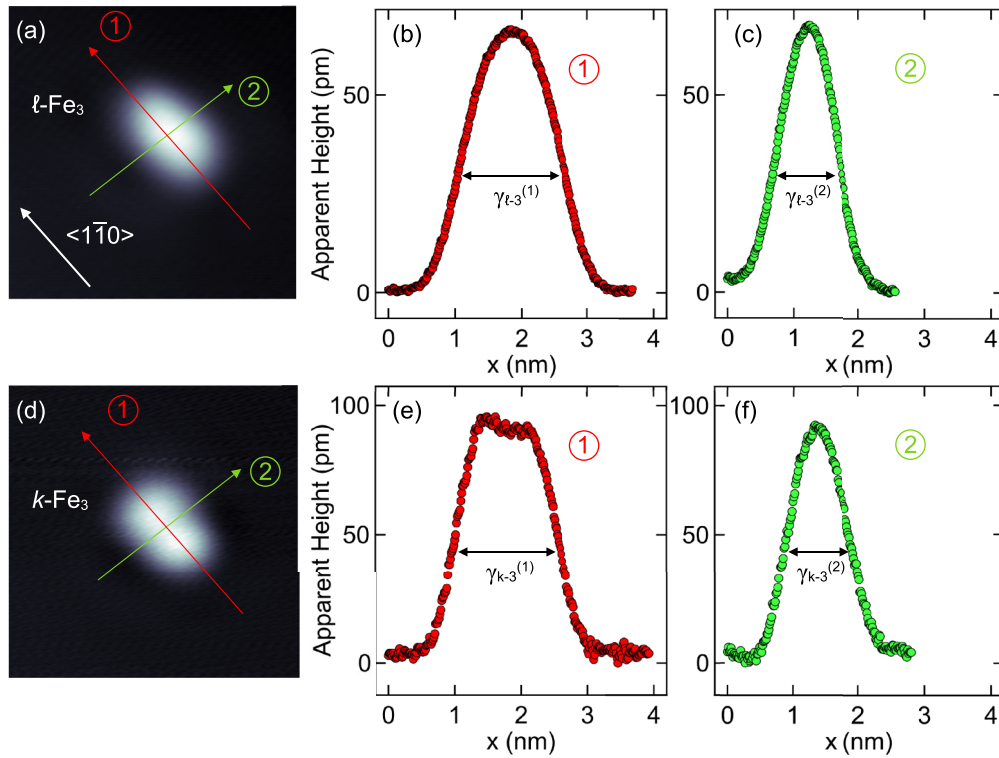


FIG. 14. (a) STM image of a linear l -Fe₃ cluster (100 mV, 100 pA, 5.3 nm × 5.3 nm) with marked directions 1 (parallel to $\langle 1\bar{1}0 \rangle$) and 2 (parallel to $\langle 11\bar{2} \rangle$). (b), (c) Cross-sectional profiles acquired along 1 and 2 marked in (a) with $\gamma_{l-3}^{(1)} \approx 1.54$ nm, $\gamma_{l-3}^{(2)} \approx 0.98$ nm, and $h_{l-3} \approx 67$ pm. (d) As in panel (a) for a kinked k -Fe₃ cluster. (e) and (f) as in (b) and (c) for the kinked trimer and directions 1, 2 marked in (c) with $\gamma_{k-3}^{(1)} \approx 1.62$ nm, $\gamma_{k-3}^{(2)} \approx 1.04$ nm and the apparently highest elevation of ≈ 95 pm.

with experimental topographs (Figs. 12–14) corroborates the suggested Fe adsorption sites and cluster geometries.

Figure 12(a) shows an STM image of Pb(111) covered with a few Fe monomers, while Fig. 12(b) presents a cross-sectional profile acquired atop three adjacent terraces [right inset to Fig. 12(a)]. The measured step height d was set to the expected geometrical distance between two subsequent (111) lattice planes, i.e., $d = a/\sqrt{3}$ with $a = 492$ pm the Pb lattice constant. Single Fe atoms appear as circular protrusions [left inset to Fig. 12(a)] with an apparent height of $h_1 \approx 45$ pm and a full width at half maximum of their cross-sectional profile of $\gamma_1 \approx 0.95$ nm [inset to Fig. 12(b)]. Occasionally, buried cavities [53–60] were signaled in STM images by their characteristic interference pattern [upper right of Fig. 12(a)]. The edges of these patterns are oriented along $\langle 1\bar{1}0 \rangle$ directions.

Dimers (Fe₂) exhibit an apparent height of $h_2 \approx 85$ pm (Fig. 13). Their circumference deviates slightly from a circle with width along $\langle 1\bar{1}0 \rangle$ of $\gamma_2^{(1)} \approx 0.99$ nm and a width of $\gamma_2^{(2)} \approx 1.08$ nm along the perpendicular direction, $\langle 11\bar{2} \rangle$. The

nearly circular protrusion is likely due to the constituent Fe atoms of the dimer occupying adjacent hcp and fcc sites, which is corroborated by the DFT calculations of the relaxed adsorption geometry.

The l -Fe₃ clusters are oriented along $\langle 1\bar{1}0 \rangle$ [Fig. 14(a)]. They exhibit an apparent height of $h_{l-3} \approx 67$ pm and a width along $\langle 1\bar{1}0 \rangle$ of $\gamma_{l-3}^{(1)} \approx 1.54$ nm [Fig. 14(b)]; their width along $\langle 11\bar{2} \rangle$ is $\gamma_{l-3}^{(2)} \approx 0.98$ nm [Fig. 14(c)]. The apparent length along $\langle 1\bar{1}0 \rangle$ is compatible with Fe atoms of the linear cluster occupying adjacent hcp sites of Pb(111) whose mutual distance is 0.35 nm. Kinked Fe trimers (k -Fe₃) deviate from a uniform orientation along $\langle 1\bar{1}0 \rangle$ [Fig. 14(d)]. Cross-sectional profiles acquired along $\langle 1\bar{1}0 \rangle$ exhibit a substructure with a lower and a higher protrusion [Fig. 14(e)], which lends support to k -Fe₃ being composed of two Fe atoms residing at adjacent hcp sites like in the l -Fe₃ cluster and the third Fe atom adopting the closest fcc site. The resulting kink has an apex angle of 150°. The widths $\gamma_{k-3}^{(1)} \approx 1.62$ nm along $\langle 1\bar{1}0 \rangle$ [Fig. 14(e)] and $\gamma_{k-3}^{(2)} \approx 1.04$ nm along $\langle 11\bar{2} \rangle$ [Fig. 14(f)] are comparable to those of the linear trimer.

- [1] Y. Luh, Bound state in superconductors with paramagnetic impurities, *Acta Phys. Sin.* **21**, 75 (1965).
 [2] H. Shiba, Classical spins in superconductors, *Prog. Theor. Phys.* **40**, 435 (1968).
 [3] A. I. Rusinov, Superconductivity near a paramagnetic impurity, *JETP Lett.* **9**, 85 (1969).

- [4] J. Bardeen, L. N. Cooper, and J. R. Schrieffer, Theory of superconductivity, *Phys. Rev.* **108**, 1175 (1957).
 [5] W. Bauriedl, P. Ziemann, and W. Buckel, Electron-tunneling observation of impurity bands in superconducting manganese-implanted lead, *Phys. Rev. Lett.* **47**, 1163 (1981).

- [6] A. Yazdani, B. A. Jones, C. P. Lutz, M. F. Crommie, and D. M. Eigler, Probing the local effects of magnetic impurities on superconductivity, *Science* **275**, 1767 (1997).
- [7] S.-H. Ji, T. Zhang, Y.-S. Fu, X. Chen, X.-C. Ma, J. Li, W.-H. Duan, J.-F. Jia, and Q.-K. Xue, High-resolution scanning tunneling spectroscopy of magnetic impurity induced bound states in the superconducting gap of Pb thin films, *Phys. Rev. Lett.* **100**, 226801 (2008).
- [8] K. J. Franke, G. Schulze, and J. I. Pascual, Competition of superconducting phenomena and Kondo screening at the nanoscale, *Science* **332**, 940 (2011).
- [9] A. V. Balatsky, I. Vekhter, and J.-X. Zhu, Impurity-induced states in conventional and unconventional superconductors, *Rev. Mod. Phys.* **78**, 373 (2006).
- [10] B. W. Heinrich, J. I. Pascual, and K. J. Franke, Single magnetic adsorbates on s-wave superconductors, *Prog. Surf. Sci.* **93**, 1 (2018).
- [11] N. Hatter, B. W. Heinrich, M. Ruby, J. I. Pascual, and K. J. Franke, Magnetic anisotropy in Shiba bound states across a quantum phase transition, *Nat. Commun.* **6**, 8988 (2015).
- [12] M. Ruby, Y. Peng, F. von Oppen, B. W. Heinrich, and K. J. Franke, Orbital picture of Yu-Shiba-Rusinov multiplets, *Phys. Rev. Lett.* **117**, 186801 (2016).
- [13] D.-J. Choi, C. Rubio-Verdú, J. de Bruijckere, M. M. Ugeda, N. Lorente, and J. I. Pascual, Mapping the orbital structure of impurity bound states in a superconductor, *Nat. Commun.* **8**, 15175 (2017).
- [14] L. Farinacci, G. Ahmadi, G. Reecht, M. Ruby, N. Bogdanoff, O. Peters, B. W. Heinrich, F. von Oppen, and K. J. Franke, Tuning the coupling of an individual magnetic impurity to a superconductor: Quantum phase transition and transport, *Phys. Rev. Lett.* **121**, 196803 (2018).
- [15] L. Schneider, M. Steinbrecher, L. Rózsa, J. Bouaziz, K. Palotás, M. dos Santos Dias, S. Lounis, J. Wiebe, and R. Wiesendanger, Magnetism and in-gap states of 3d transition metal atoms on superconducting Re, *npj Quantum Mater.* **4**, 42 (2019).
- [16] M. Ruby, B. W. Heinrich, Y. Peng, F. von Oppen, and K. J. Franke, Wave-function hybridization in Yu-Shiba-Rusinov dimers, *Phys. Rev. Lett.* **120**, 156803 (2018).
- [17] D.-J. Choi, C. G. Fernández, E. Herrera, C. Rubio-Verdú, M. M. Ugeda, I. Guillamón, H. Suderow, J. I. Pascual, and N. Lorente, Influence of magnetic ordering between Cr adatoms on the Yu-Shiba-Rusinov states of the β -Bi₂Pd superconductor, *Phys. Rev. Lett.* **120**, 167001 (2018).
- [18] S. Kezilebieke, M. Dvorak, T. Ojanen, and P. Liljeroth, Coupled Yu-Shiba-Rusinov states in molecular dimers on NbSe₂, *Nano Lett.* **18**, 2311 (2018).
- [19] P. Beck, L. Schneider, L. Rózsa, K. Palotás, A. Lászlóffy, L. Szunyogh, J. Wiebe, and R. Wiesendanger, Spin-orbit coupling induced splitting of Yu-Shiba-Rusinov states in anti-ferromagnetic dimers, *Nat. Commun.* **12**, 2040 (2021).
- [20] M. E. Flatté and D. E. Reynolds, Local spectrum of a superconductor as a probe of interactions between magnetic impurities, *Phys. Rev. B* **61**, 14810 (2000).
- [21] T. Meng, J. Klinovaja, S. Hoffman, P. Simon, and D. Loss, Superconducting gap renormalization around two magnetic impurities: From Shiba to Andreev bound states, *Phys. Rev. B* **92**, 064503 (2015).
- [22] B. W. Heinrich, L. Braun, J. I. Pascual, and K. J. Franke, Tuning the magnetic anisotropy of single molecules, *Nano Lett.* **15**, 4024 (2015).
- [23] L. Malavolti, M. Briganti, M. Hänze, G. Serrano, I. Cimatti, G. McMurtrie, E. Otero, P. Ohresser, F. Totti, M. Mannini, R. Sessoli, and S. Loth, Tunable spin–superconductor coupling of spin 1/2 vanadyl phthalocyanine molecules, *Nano Lett.* **18**, 7955 (2018).
- [24] J. Homberg, A. Weismann, R. Berndt, and M. Gruber, Inducing and controlling molecular magnetism through supramolecular manipulation, *ACS Nano* **14**, 17387 (2020).
- [25] C. Li, J. Homberg, A. Weismann, and R. Berndt, On-surface synthesis and spectroscopy of aluminum phthalocyanine on superconducting lead, *ACS Nano* **16**, 16987 (2022).
- [26] A. Kamlapure, L. Cornils, R. Žitko, M. Valentyuk, R. Mozara, S. Pradhan, J. Fransson, A. I. Lichtenstein, J. Wiebe, and R. Wiesendanger, Correlation of Yu-Shiba-Rusinov states and Kondo resonances in artificial spin arrays on an s-wave superconductor, *Nano Lett.* **21**, 6748 (2021).
- [27] J. Li, T. Neupert, Z. Wang, A. H. MacDonald, A. Yazdani, and B. A. Bernevig, Two-dimensional chiral topological superconductivity in Shiba lattices, *Nat. Commun.* **7**, 12297 (2016).
- [28] G. Kresse and J. Furthmüller, Efficient iterative schemes for ab initio total-energy calculations using a plane-wave basis set, *Phys. Rev. B* **54**, 11169 (1996).
- [29] G. Kresse and J. Furthmüller, Efficiency of ab-initio total energy calculations for metals and semiconductors using a plane-wave basis set, *Comput. Mater. Sci.* **6**, 15 (1996).
- [30] L. Limot, J. Kröger, R. Berndt, A. Garcia-Lekue, and W. A. Hofer, Atom transfer and single-atom contacts, *Phys. Rev. Lett.* **94**, 126102 (2005).
- [31] J. Kröger, H. Jensen, and R. Berndt, Conductance of tip–surface and tip–atom junctions on Au(111) explored by a scanning tunnelling microscope, *New J. Phys.* **9**, 153 (2007).
- [32] J. Kröger, N. Néel, A. Sperl, Y. F. Wang, and R. Berndt, Single-atom contacts with a scanning tunnelling microscope, *New J. Phys.* **11**, 125006 (2009).
- [33] J. Kröger, N. Néel, and L. Limot, Contact to single atoms and molecules with the tip of a scanning tunnelling microscope, *J. Phys.: Condens. Matter* **20**, 223001 (2008).
- [34] R. Berndt, J. Kröger, N. Néel, and G. Schull, Controlled single atom and single molecule contacts, *Phys. Chem. Chem. Phys.* **12**, 1022 (2010).
- [35] M. Müller, C. Salgado, N. Néel, J. J. Palacios, and J. Kröger, Plasticity of single-atom Pb junctions, *Phys. Rev. B* **93**, 235402 (2016).
- [36] D. M. Ceperley and B. J. Alder, Ground state of the electron gas by a stochastic method, *Phys. Rev. Lett.* **45**, 566 (1980).
- [37] B. Nyári, A. Lászlóffy, L. Szunyogh, G. Csire, K. Park, and B. Ujfalussy, Relativistic first-principles theory of Yu-Shiba-Rusinov states applied to Mn adatoms and Mn dimers on Nb(110), *Phys. Rev. B* **104**, 235426 (2021).
- [38] M. E. Flatté and J. M. Byers, Local electronic structure of a single magnetic impurity in a superconductor, *Phys. Rev. Lett.* **78**, 3761 (1997).
- [39] M. E. Flatté and J. M. Byers, Local electronic structure of defects in superconductors, *Phys. Rev. B* **56**, 11213 (1997).
- [40] J. Bauer, J. I. Pascual, and K. J. Franke, Microscopic resolution of the interplay of Kondo screening and superconducting

- pairing: Mn-phthalocyanine molecules adsorbed on superconducting Pb(111), *Phys. Rev. B* **87**, 075125 (2013).
- [41] R. Žitko, J. S. Lim, R. López, and R. Aguado, Shiba states and zero-bias anomalies in the hybrid normal-superconductor Anderson model, *Phys. Rev. B* **91**, 045441 (2015).
- [42] D. K. Morr and N. A. Stavropoulos, Quantum interference between impurities: Creating novel many-body states in *s*-wave superconductors, *Phys. Rev. B* **67**, 020502(R) (2003).
- [43] D. K. Morr and J. Yoon, Impurities, quantum interference, and quantum phase transitions in *s*-wave superconductors, *Phys. Rev. B* **73**, 224511 (2006).
- [44] G. C. Ménard, S. Guissart, C. Brun, S. Pons, V. S. Stolyarov, F. Debontridder, M. V. Leclerc, E. Janod, L. Cario, D. Roditchev, P. Simon, and T. Cren, Coherent long-range magnetic bound states in a superconductor, *Nat. Phys.* **11**, 1013 (2015).
- [45] J. Tersoff and D. R. Hamann, Theory and application for the scanning tunneling microscope, *Phys. Rev. Lett.* **50**, 1998 (1983).
- [46] J. Tersoff and D. R. Hamann, Theory of the scanning tunneling microscope, *Phys. Rev. B* **31**, 805 (1985).
- [47] R. C. Dynes, V. Narayanamurti, and J. P. Garno, Direct measurement of quasiparticle-lifetime broadening in a strong-coupled superconductor, *Phys. Rev. Lett.* **41**, 1509 (1978).
- [48] S. Loth, S. Baumann, C. P. Lutz, D. M. Eigler, and A. J. Heinrich, Bistability in atomic-scale antiferromagnets, *Science* **335**, 196 (2012).
- [49] I. Giaever, Energy gap in superconductors measured by electron tunneling, *Phys. Rev. Lett.* **5**, 147 (1960).
- [50] S. Schulte, N. Néel, L. Rózsa, K. Palotás, and J. Kröger, Changing the interaction of a single-molecule magnetic moment with a superconductor, *Nano Lett.* **23**, 1622 (2023).
- [51] L. N. Oliveira, E. K. U. Gross, and W. Kohn, Density-functional theory for superconductors, *Phys. Rev. Lett.* **60**, 2430 (1988).
- [52] J. Minár, O. Šipr, J. Braun, and H. Ebert, KKR Green's function method in reciprocal and real space, in *Multiple Scattering Theory for Spectroscopies*, edited by D. Sébilleau, K. Hatada, and H. Ebert (Springer International Publishing, Cham, 2018), pp. 93–142.
- [53] M. Schmid, W. Hebenstreit, P. Varga, and S. Crampin, Quantum wells and electron interference phenomena in Al due to subsurface noble gas bubbles, *Phys. Rev. Lett.* **76**, 2298 (1996).
- [54] O. Kurnosikov, O. A. O. Adam, H. J. M. Swagten, W. J. M. de Jonge, and B. Koopmans, Probing quantum wells induced above a subsurface nanocavity in copper, *Phys. Rev. B* **77**, 125429 (2008).
- [55] O. Kurnosikov, D. V. Kulikov, V. S. Kharlamov, H. J. M. Swagten, and Yu. V. Trushin, Temperature-induced evolution of subsurface nanocavities in argon-implanted copper, *Phys. Rev. B* **84**, 054109 (2011).
- [56] O. Kurnosikov, J. H. Nietsch, M. Sicot, H. J. M. Swagten, and B. Koopmans, Long-range electron interferences at a metal surface induced by buried nanocavities, *Phys. Rev. Lett.* **102**, 066101 (2009).
- [57] C. Sprodowski and K. Morgenstern, Three types of bulk impurity induced interference patterns on the (100) and (111) faces of Ne- and Ar-doped silver, *Phys. Rev. B* **82**, 165444 (2010).
- [58] O. Kurnosikov, H. J. M. Swagten, and B. Koopmans, Internal electron diffraction from atomically ordered subsurface nanostructures in metals, *Phys. Rev. Lett.* **106**, 196803 (2011).
- [59] M. Müller, N. Néel, S. Crampin, and J. Kröger, Lateral electron confinement with open boundaries: Quantum well states above nanocavities at Pb(111), *Phys. Rev. Lett.* **117**, 136803 (2016).
- [60] M. Müller, N. Néel, S. Crampin, and J. Kröger, Open-boundary reflection of quantum well states at Pb(111), *Phys. Rev. B* **96**, 205426 (2017).